

# Modelling snow melt and snowcover depletion in a small alpine cirque, Canadian Rocky Mountains

Christopher M. DeBeer\* and John W. Pomeroy

*Centre for Hydrology, University of Saskatchewan, 117 Science Place, Saskatoon, Saskatchewan, Canada*

## Abstract:

Spatial and temporal patterns of areal snowcover depletion (SCD) were studied over a small (<0.6 km<sup>2</sup>) alpine cirque within the Canadian Rocky Mountains using a combined approach of daily acquisition of remotely sensed imagery, together with meteorological observations and snowmelt modelling. Digital terrestrial photographs were georeferenced using a novel software tool together with a high-resolution digital elevation model and used to derive measurements of fractional snowcovered area (SCA) over the cirque. Manual snow surveys carried out in the pre-melt period were used to describe the initial frequency distribution of snow water equivalent (SWE) values over the cirque, and indicated a lognormal distribution of SWE when surveys were stratified by terrain features. Rates of snowmelt were simulated using a physically based snowmelt energy balance model, Snobal, driven by observed meteorological conditions at a nearby station, which were adjusted for slope orientation and exposure by making corrections to observed incoming shortwave and longwave radiation components in the cold regions hydrological model platform. Simulated melt rates were then applied to the approximated SWE distributions to model the decline in SCA over the spring. The model was found to perform well for the simulation of snowmelt based on point observations of SWE at the meteorological station, and produced a close correspondence between simulated and observed SCD curves representing two opposing slopes within the cirque. The results show that both the pre-melt distributions of SWE and the spring melt rates exhibit considerable spatial variability between distinct slope units within the cirque, and that this variability has a significant impact on simulated SCD. Assuming a unimodal pre-melt frequency distribution and conditions of spatially uniform snowmelt over complex terrain such as this can lead to large errors in the simulation results. It is suggested that modelling applications intended to represent snowmelt dynamics and areal SCD in similar alpine environments consider the effects of spatial variation in SWE distribution and melt energetics between slopes. Copyright © 2009 John Wiley & Sons, Ltd.

KEY WORDS snowcover depletion; snowmelt modelling; scaling; mountain hydrology; spatial variability

Received 30 June 2008; Accepted 25 March 2009

## INTRODUCTION

In alpine environments, variations in elevation, slope, aspect, topographic shelter and vegetation structure give rise to complex patterns of both snowcover development throughout the winter and surface energetics during melt (Elder *et al.*, 1991, 1998; Pomeroy, 1991; Blöschl and Kirnbauer, 1992; Allen and Walsh, 1993; Marks *et al.*, 1998; Marks and Winstral, 2001; Pomeroy *et al.*, 2003; Anderton *et al.*, 2004). These patterns largely control the dynamics of areal snowcover depletion (SCD) over the landscape during the spring and result in a multitude of snow patches of varying size with intervening snow-free areas as the snowcover ablates. This disintegration of the snowpack into patches over time is important hydrologically as it controls the contributing area for snowmelt runoff generation and thereby affects the rate and magnitude of meltwater production. From a climatological perspective, the fraction of snowcovered area (SCA) is significant as it exerts a major influence on the surface energy fluxes through its effects on the albedo and

temperature of the surface. Accurate representation of SCA and SCD is therefore important for hydrological and atmospheric modelling applications in such environments.

One approach is to explicitly model the spatial and temporal variability in snow processes at very fine scales using fully distributed models (e.g. Davis *et al.*, 1995; Hartman *et al.*, 1999; Marks *et al.*, 1999). These models can be run at spatial scales as small as several meters; however, this level of detail necessitates extensive spatial information on model parameters and forcing variables and requires considerable computing resources. For these reasons, the approach is limited to a relatively small number of applications for which these requirements are met.

More commonly, hydrological models and land surface schemes are applied at larger spatial scales and account for the variability at small scales by employing a sub-grid or sub-model element parameterization of the areal snowcover state. This allows for the determination of effective surface parameters or for weighting separate flux calculations for snowcovered and snow-free areas. These parameterizations are often based on mean snow water equivalent (SWE) or accumulated depth of snowmelt over time, and rely on some understanding

\* Correspondence to: Christopher M. DeBeer, Centre for Hydrology, University of Saskatchewan, 117 Science Place, Saskatoon, Saskatchewan S7N 5C8, Canada. E-mail: cmd225@mail.usask.ca

of the frequency distribution of SWE over the landscape. The approach generally relies on several limiting assumptions, however, including spatially uniform melt rates over the model domain or computational grid cell area (Liston, 1999; Luce *et al.*, 1999; Luce and Tarboton, 2004), some theoretical average depth of snow beyond which fractional SCA is equal to unity (Donald *et al.*, 1995) or a single unimodal frequency distribution of SWE over the grid cell (Liston, 2004). Even at relatively small spatial scales in sharp alpine terrain, these assumptions are often violated, and thus the applicability of models relying on such parameterizations is potentially limited. The problem is related, in part, to the choice of grid cell resolution or the method of disaggregation of the terrain for modelling. The use of an arbitrary grid system that does not conform to natural scales and location of variability (both stochastic and deterministic) in the processes being modelled (e.g. Seyfried and Wilcox, 1995) introduces artificial scaling problems in the models where none exists in nature, and thus sophisticated techniques must be employed to handle the variability at sub-grid scales. The processes involved in areal SCD generally do not aggregate linearly and it is not possible to assume that  $E(f(x)) = f(E(x))$ , where  $E$  is the mathematical expectation (i.e. mean),  $x$  is location and  $f$  a function or variable (Blöschl, 1999). This must be considered when changing model scales and/or lumping together model inputs and conditions over larger computational areas. It is likely that hydrological modelling applications dealing with snowmelt and areal SCD can be applied at intermediate spatial scales and objectively chosen terrain units for calculation, which are consistent with the variability in the relevant processes, and thereby avoid resorting to the use of finely distributed approaches or arbitrarily selected model grids. Several recent studies (e.g. Pomeroy *et al.*, 2004; Davison *et al.*, 2006; Dornes *et al.*, 2008) have focused on the appropriate scale and/or landscape segmentation for dealing with snow ablation, SCD and meltwater runoff generation. These studies have shown that these processes are terrain-class-specific, and that stratification of the landscape according to features such as slope/aspect and elevation yields improved simulation results relative to those from an inappropriately segmented or spatially aggregated treatment of the processes.

This study aims to build on these findings and explore the effects of spatial variability in the relevant processes for areal SCD in a region of sharp alpine topography in the Canadian Rocky Mountains. We demonstrate the use of a relatively new technique—oblique terrestrial photography—for deriving daily measurements of SCA in this environment, where conventional remote sensing methods are unfeasible due to persistent cloud cover and infrequent return intervals of most sensors. The specific objective of this study is to upscale a physically based point-scale energy balance simulation of snowmelt to calculate the basin scale SCA and SCD as well as that for two distinct and opposing slope units within the small basin. We use these simulations to assess the modelling

implications of spatially variable SWE and snowmelt rates within this environment.

### THEORETICAL CONSIDERATIONS

#### *The lognormal probability density function*

As a result of differences in snow deposition and redistribution of snow over a landscape, snowcovers tend to exhibit substantial spatial variability in their water equivalent depth. A number of studies within a variety of environments (e.g. Donald *et al.*, 1995; Shook, 1995; Pomeroy *et al.*, 1998, 2001; Faria *et al.*, 2000) have found that distributions of SWE prior to melt can be approximated by the lognormal distribution when stratified by terrain classes. The lognormal distribution has the advantage that it is a relatively simple two-parameter distribution with known statistical properties.

The lognormal distribution is expressed in terms of the probability density function of the transformed variable, i.e.  $y = \ln(\text{SWE})$  as in the following Equation (1):

$$f(y) = \frac{1}{s_y^2 \sqrt{2\pi}} \exp\left(-\frac{(y - \bar{y})^2}{2s_y^2}\right), \quad (1)$$

where  $\bar{y}$  is the mean of the logarithmic values of SWE and  $s_y$  is the standard deviation of the transformed variable. For practical applications, the lognormal distribution is often expressed in the following linear form:

$$\text{SWE} = \overline{\text{SWE}}(1 + KCV), \quad \text{or} \quad (2a)$$

$$\text{SWE} = \overline{\text{SWE}} + Ks, \quad (2b)$$

where SWE is the value of the snow water equivalent having an exceedence probability equal to that of the frequency factor,  $K$  and  $\overline{\text{SWE}}$ ,  $s$  and  $CV$  are the arithmetic mean, standard deviation and coefficient of variation (i.e. standard deviation divided by the mean) of the natural values, respectively. When the values of the transformed variable are normally distributed,  $K$  in Equation (2) is the well-known  $z$ -statistic of the normal distribution and is given by the following Equation (3) (Chow, 1954):

$$K = \frac{1}{CV} \left[ \exp\left(s_y K_y - \frac{s_y^2}{2}\right) - 1 \right], \quad (3)$$

where  $K_y = (y - \bar{y})/s_y$ , the theoretical frequency factor of the transformed data.

Equation (2) describes the theoretical two-parameter lognormal distribution. Thus, observed values of SWE plotted against  $K$  should approximate a straight line with a slope equal to the standard deviation of SWE and an intercept at  $K = 0$  equal to  $\overline{\text{SWE}}$ , provided that the underlying distribution is lognormal. Note that natural values of  $K$  and SWE should be used. Values of  $K$  for observed data (excluding observations of zero SWE depth) can be calculated as (Chow, 1954):

$$K = \frac{\exp\left(s_y K_y - \frac{s_y^2}{2}\right) - 1}{\sqrt{\exp(s_y^2) - 1}}. \quad (4)$$

A value for observed  $K_y$  is required for Equation (4); this may be determined by noting that the exceedence probability,  $P$ , of  $K_y$  and SWE are equal for a given sample of  $n$  observations. The probability of  $K_y$  being exceeded,  $P(K_y)$ , is provided in the Equation (5):

$$P(K_y) = \frac{1}{\sqrt{2\pi}} \int_{K_y}^{\infty} \exp\left(-\frac{K_y^2}{2}\right) dK_y. \quad (5)$$

The exceedence probability of each measurement for a set of observations of SWE can be determined following Gumbel (1954) as in the following Equation (6):

$$P(\text{SWE}) = \frac{r}{n+1}, \quad (6)$$

where  $r$  is the rank of the SWE observation when arranged in decreasing order of magnitude and  $n$  is the number of observations. In Equation (6), observations of zero SWE depths should be included. Given that  $P(\text{SWE}) = P(K_y)$ , corresponding values for observed  $K_y$  can be determined by taking the inverse of the standard normal cumulative distribution for the values of  $1 - P(\text{SWE})$  for each SWE observation (e.g.  $P(\text{SWE})$  is the exceedence probability and therefore  $1 - P(\text{SWE})$  is the cumulative probability).

#### Areal SCD

Approximations of the snowcover distribution based on the lognormal probability density function are well suited for the calculation of SCA and SCD over a given terrain unit. For example, as expressed by Equation (2), the value of  $K$  is a function of the exceedence probability of the corresponding value of SWE. Therefore, the frequency factor corresponding to specific SWE values can be used as an index of the probability of that particular value of SWE being exceeded, or alternatively, the areal fraction of the snowcover with a value of SWE exceeding that particular value. The value of  $K$  corresponding to  $\text{SWE} = 0$  (i.e.  $K_{\min}$ ) is then an index of the SCA over the landscape.

Estimates of SCA and SCD can be derived as a function of the applied melt (i.e. the one-dimensional melt rate applied uniformly to the SWE distribution) and the initial frequency distribution of SWE. The steps involved in this procedure are as follows:

1. Establish the values of  $\overline{\text{SWE}}$  and CV, and from Equation (2) the value of  $K_{\min}$  is determined from the corresponding  $x$ -intercept (i.e.  $\text{SWE} = 0$ ).
2. Calculate  $K_y$  from Equation (4). This requires the standard deviation of the log-transformed data, which can be estimated from (Chow, 1954):

$$s_y = \sqrt{\ln(\text{CV}^2 + 1)}. \quad (7)$$

3. Based on this estimate of  $K_y$ , the SCA fraction (equivalent to  $P(\text{SWE})$ ) is quantified as  $P(K_y)$ , which is determined as one minus the value of the standard

normal cumulative distribution function evaluated for  $K_y$ .

4. For the next time step, the value of  $\overline{\text{SWE}}$  is reduced by the amount of applied melt, and the procedure is subsequently repeated.

This procedure is equivalent to uniformly melting the initial frequency distribution of SWE.

## METHODS

### Study site

This work focused on a small ( $\sim 0.6 \text{ km}^2$ ) alpine cirque on the eastern side of Mt. Allan (hereafter referred to as Mt. Allan cirque) within the Marmot Creek Research Basin ( $50.96^\circ \text{N}$ ;  $115.21^\circ \text{W}$ ). The cirque ranges in elevation from  $\sim 2300 \text{ m}$  at local treeline up to  $2831 \text{ m}$  at the summit of Mt. Allan, and is characterized by several major slopes of different orientation with distinct microtopographic variations superimposed over the terrain (Figure 1). Marmot Creek is situated within the Front Ranges of the Canadian Rockies, where climatic conditions are dominated by continental air masses. Winters are long and cold, with an average temperature of  $-15^\circ \text{C}$  for the months of January through March (i.e. for Mt. Allan cirque based on extrapolated readings from Kananaskis, AES Sta. 3053600;  $1391 \text{ m}$ ). The spring season is generally cool and wet, often producing late snowfall events at high elevations. Average temperatures at the Mt. Allan cirque for May and June (during the primary snowmelt period) are  $2$  and  $8^\circ \text{C}$ , respectively. Historically, annual precipitation at Marmot Creek has been observed to average about  $900 \text{ mm}$ , increasing to over  $1140 \text{ mm}$  at treeline near Mt. Allan cirque (Storr, 1967), and recent observations more-or-less correspond to these values. Roughly  $60\text{--}75\%$  of the total precipitation falls as snow at Marmot Creek, while at the higher elevations here this fraction is likely greater.

Meteorological observations during the course of this study were made at a permanent meteorological station located on Fisera Ridge directly adjacent to the cirque ( $2318 \text{ m}$ ; Figure 1). Incoming shortwave radiation was measured here using a Kipp & Zonen CM21 pyranometer (directional error  $< \pm 10 \text{ W/m}^2$ ), and incoming longwave radiation was measured using a Kipp & Zonen CG1 pyrgeometer (manufacturer estimated error  $< \pm 20 \text{ W/m}^2$ ). Air temperature and relative humidity were measured with a Vaisala HMP45C212 hygrothermometer housed inside a Gill radiation shield. Wind speed and direction were measured using an R.M. Young anemometer (Model 05103-10). The hygrothermometer and anemometer were mounted at respective heights of  $2.25$  and  $2.55 \text{ m}$  above the ground surface. Rainfall was measured at Fisera Ridge using a Campbell Scientific TB4-L tipping bucket rain gauge, while snowfall depths were measured with a Campbell Scientific SR50 sonic ranging sensor. Measurements of total precipitation were obtained using a Geonor T-200B strain gauge located at the mid-elevation Upper

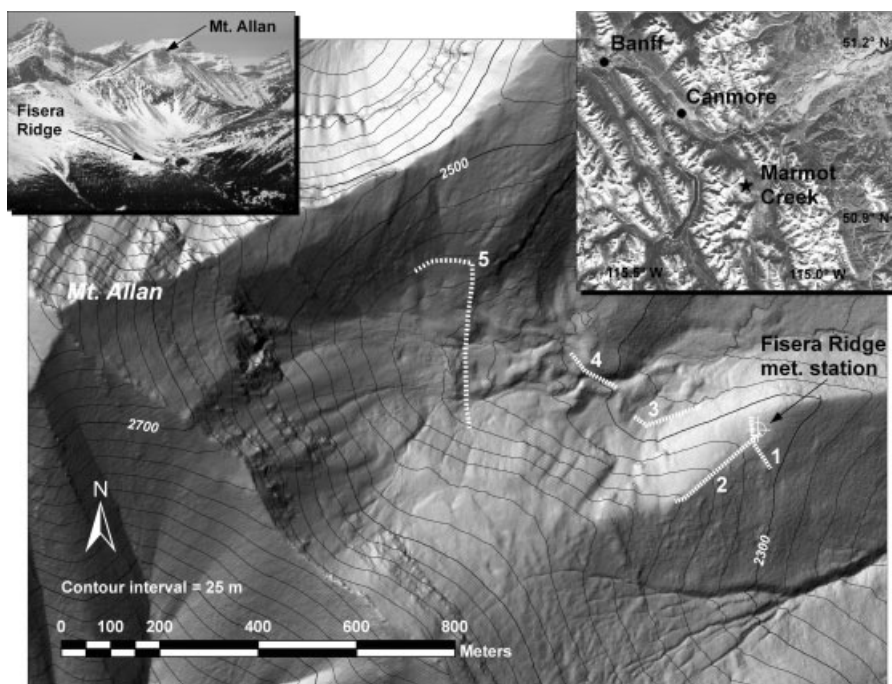


Figure 1. Shaded relief map of the Mt. Allan cirque within the Marmot Creek Research Basin, Kananaskis, Alberta. Snow survey transects are marked on the map (white dashed lines) along with the location of the meteorological station on Fisera Ridge (hatched circle). Map insets include an oblique aerial photograph of the cirque and a Landsat 7 image showing the location of Marmot Creek within the Rocky Mountain Front Ranges

Clearing site (1843 m) within the Marmot Creek basin roughly 2 km away.

#### *Terrestrial photography acquisition and image analysis*

In early May of 2007, a digital single lens reflex camera (Pentax model K110D) with a high-precision lens to minimize radial image distortion (Pentax DA 21 mm F3.2AL Limited) was mounted to the Fisera Ridge station inside a weatherproof housing. The camera's shutter release was controlled remotely using a Campbell Scientific CR23X datalogger, which was programmed to take photos several times daily. Photos taken at 12:00 p.m. local time each day were selected for analysis, except in situations when low cloud cover or snowfall obscured the terrain.

To derive SCA measurements from the digital photography, the images were projected orthogonally onto a 1-m resolution digital elevation model (DEM) that was generated from airborne LiDAR (Light Detection And Ranging) data collected in August 2007 over the entire Marmot Creek Research Basin. The re-projection of these images was performed using an IDL software tool, *Georeferencing Terrestrial Photography*, described in detail by Corripio (2004). Initially, the DEM is projected virtually from the perspective of the camera position and orientation so that it forms a two-dimensional representation of the relief information contained in the DEM. Orientation data consisting of three rotation parameters for spatial rotations of the camera, location of the camera ( $x$ ,  $y$ ,  $z$ ) and the central pixel of the photographic image in the DEM coordinate system and principal distance (i.e. camera focal length) are required to achieve this representation. This virtual projection of the DEM is then scaled

by the resolution of the image, and the correspondence between image pixels, the projected coordinates of the DEM cells and their geographic location is established. Finally, based on this information, the image pixels are re-projected over the DEM to the geographic location that they correspond to.

Orientation parameters were derived manually by trial and error for each image to achieve optimal correspondence between the image pixels and their geographic coordinates. This was necessary since very subtle movements of the camera due to wind and periodic operator access into the camera housing caused significant movements of the geographic locations of individual pixels between subsequent images. Comparison of a series of ground control points within the cirque obtained using a differential global positioning system and clearly identifiable objects within the georeferenced images (e.g. bushes, small rock outcrops, etc.) revealed a root mean square (RMS) error of  $\sim 3$  m, but this error tended to be directionally consistent, and thus the area of features was preserved. Visual inspection of the georeferenced image series and a 1-m resolution shaded relief image of the DEM also indicated a very close correspondence between data sets over nearly all visible parts of the cirque.

Daily SCA measurements were derived from the georeferenced imagery for the entire cirque as well as for two opposing slopes within the cirque (described in more detail below). These measurements were made using ESRI ArcMap 9.1, in which a threshold was applied to classify snow and non-snow areas. This classification could be easily performed because of the large difference in brightness values of the pixels representing snow and those representing bare ground or vegetation. SCA was

then determined as the ratio of the number of 'snow' pixels to the total number of pixels over the relevant area (excluding pixels containing 'no-data' values that were hidden from view of the camera).

#### Pre-melt snow surveys

Multiple snow surveys were carried out along linear transects within and adjacent to the cirque on March 29–30 before the main snowmelt period to characterize the distribution of pre-melt SWE (Figure 1). Each of these surveys included between 25 and 100 measurements of snow depth obtained using an aluminium rod graduated in 1 cm increments and density measurements taken every fifth-depth measurement using a Mount Rose snow tube. In addition, several measurements of the density of shallow snow were made by weighing samples obtained with a fixed volume triangular cutting device (Perla 'Swedish Sampler'). The surveys were chosen within a variety of terrain types across the cirque to obtain representative distributions of SWE for the major topographic slope, aspect and exposure classes within the cirque. Subsequent analysis of these data was carried out to determine the relevant statistical parameters (i.e.  $\overline{\text{SWE}}$  and CV) and test the applicability of the lognormal distribution for describing pre-melt SWE within the cirque.

#### Snowmelt modelling and SCD simulation

Snowmelt rates were simulated within the cirque using the cold regions hydrological model (CRHM) platform (Pomeroy *et al.*, 2007). CRHM is a flexible object-oriented modelling system that can be used to develop, support and apply dynamic hydrological process algorithms. These algorithms are applied over hydrological response units (i.e. homogeneous terrain units characterized by their geometric and surface vegetation properties), within which conditions and processes are represented by single sets of parameters, state variables and energy and mass fluxes. Various component modules representing basin characteristics, observations and hydrological processes are combined within CRHM to form an operational model of the system that has a level of complexity specified by the needs of the user.

Melt rates were computed using the Snobal (snowmelt energy balance model) (Marks *et al.*, 1998, 1999) module within CRHM. This module approximates the snowcover as being composed of two layers: a surface active layer of fixed thickness and a lower layer representing the remaining snowpack. The module solves for the temperature ( $^{\circ}\text{C}$ ) and the specific mass ( $\text{kg/m}^2$ ) or water equivalent depth per unit area (mm) of each layer for each timestep. The energy balance of the snowpack at a point is expressed as in the following Equation (8):

$$Q_m = Q^* + Q_H + Q_E + Q_G + Q_P - dU/dt, \quad (8)$$

where  $Q_m$  is the energy available for snowmelt,  $Q^*$  is the net radiation composed of both shortwave and longwave components,  $Q_H$ ,  $Q_E$  and  $Q_G$  are the sensible, latent

and ground heat fluxes, respectively,  $Q_P$  is the energy added to the snowpack by precipitation, and  $U$  is the internal energy of the snowpack. The melt energy can be expressed as a depth of melt,  $m$ , by the following Equation (9):

$$m = \frac{Q_m}{\rho h_f \beta}, \quad (9)$$

where  $\rho$  is the density of the snow,  $h_f$  is the latent heat of fusion (0.334 MJ/kg) and  $\beta$  is the fraction of ice in snow (taken as 0.97). Melt is computed in either layer when the accumulated energy exceeds that required to bring the snowpack to  $0^{\circ}\text{C}$ , at which point positive values of  $Q_m$  result in snowmelt. The reader is referred to Marks *et al.* (1998, 1999) for a comprehensive description of the Snobal model.

The model was run in CRHM using observed meteorological conditions from Fisera Ridge at 15-min time intervals as external forcing data. Melt rates were computed at a point from these data, and water equivalent melt depths were summed over 24-h periods to produce values of the simulated daily melt rate. These computations were also made for two opposing major slopes within the cirque. The first of these is a predominantly north-facing slope ranging in elevation from 2325 to 2440 m situated on the southern side of the cirque. The other slope faces south to south-east and ranges in elevation from 2375 to 2500 m. These slopes were distinguished on the basis of dominant terrain features (i.e. slope, aspect, elevation, exposure) that exhibit a relatively large degree of homogeneity over the defined areas. Table I lists several of the relevant terrain parameters used to define each of the slope units.

To simulate melt rates over the north- and south-facing slopes, the direct and diffuse beam components of solar radiation were adjusted using the modules *Global* and *Slope\_Qsi* within CRHM. *Global* calculates the theoretical direct beam component of solar radiation to slopes,  $Q_{\text{dir}}$ , using an expression proposed by Garnier and Ohmura (1970) as in the Equation (10):

$$\begin{aligned} Q_{\text{dir}} = I \cdot p^m [ & (\sin \theta \cos H)(-\cos A \sin Z) \\ & - \sin H(\sin A \cos Z) \\ & + (\cos \theta \cos H) \cos Z] \cos \delta + [\cos \theta (\cos A \sin Z) \\ & + (\sin \theta \cos Z)] \sin \delta \end{aligned} \quad (10)$$

Table I. Terrain parameters for the two slopes within the Mt. Allan cirque and for the point location of the Fisera Ridge meteorological station

Parameter	North-facing slope	South-facing slope	Met station
Average slope ( $^{\circ}$ )	30	23	0
Average aspect ( $^{\circ\text{a}}$ )	20	160	NA
Median elevation (m)	2382	2438	2318
Sky view factor	0.62	0.66	0.74

<sup>a</sup> Units are degrees clockwise from North.

where  $I$  is the intensity of extraterrestrial radiation,  $p$  is the mean zenith path transmissivity of the atmosphere,  $m$  is the optical air mass,  $\delta$  is the declination of the sun,  $\theta$  is the latitude,  $H$  is the hour angle measured from solar noon positively towards west,  $A$  is the slope azimuth (i.e. aspect) measured from the north through east and  $Z$  is the angle of the slope. *Global* uses a simple means of calculating the diffuse clear-sky radiation,  $Q_{\text{dif}}$  ( $\text{W}/\text{m}^2$ ), given by List (1968) as in the following Equation (11):

$$Q_{\text{dif}} = 0.5((1 - aw - ac)Q_{\text{ext}} - Q_{\text{dir}}), \quad (11)$$

where  $aw$  is the radiation absorbed by water vapour (7%),  $ac$  is the radiation absorbed by ozone (2%),  $Q_{\text{ext}}$  ( $\text{W}/\text{m}^2$ ) is the extraterrestrial radiation on a horizontal surface at the outer limit of the earth's atmosphere and  $Q_{\text{dir}}$  ( $\text{W}/\text{m}^2$ ) is the direct clear-sky radiation reaching the earth's surface on a horizontal surface. The *Slope-Qsi* module estimates shortwave radiation for a slope from the measured incoming shortwave radiation on the level. The ratio of measured shortwave radiation and the calculated theoretical clear-sky direct and diffuse radiation on a horizontal plane is used to adjust the calculated clear-sky shortwave radiation value on the slope.

The snow albedo,  $\alpha$ , was parameterized as an exponential decay during the melt period to an asymptotic minimum of 0.3 following Essery and Etchevers (2004). For each timestep with snowmelt, the albedo is updated according to the Equation (12):

$$\alpha \longrightarrow (\alpha - 0.3) \exp\left(\frac{-\Delta t}{\tau}\right) + 0.3, \quad (12)$$

where  $\Delta t$  is the timestep length and  $\tau$  is a time constant applied to melting snow. We used a value of  $10^6$  s for  $\tau$  in our model. For time steps with snowfall, the albedo is increased by the following Equation (13):

$$\alpha \longrightarrow \alpha + (\alpha_f - \alpha) \frac{S_f \Delta t}{10}, \quad (13)$$

where  $S_f$  is the snowfall rate ( $\text{mm}/\Delta t$ ), so that a 10 mm snowfall refreshes the albedo to  $\alpha_f$  (set equal to 0.85 in our model). This parameterization allows the albedo of snow to decline to artificially low values for pure snow, but in doing so, it effectively represents an areal albedo that is characteristic of the mixed snow, vegetation and bare ground surface supplying energy to the melting snow. Further refinements to the modelling should include explicit representation of small-scale advection. Our observations within the cirque also indicate that such low values are not unrealistic as the snowcover here is covered in wind-blown debris and snow algae during the late spring, which significantly reduced the albedo of the snow.

Incoming longwave radiation was adjusted for the slopes using a modified version of the parameterization suggested by Sicart *et al.* (2006), in which the effect of varying sky view is accounted for. The sky view factor is the fraction of sky visible from a specific point, and is defined as the ratio of the projected area

of the visible hemisphere to the projected area of the whole hemisphere. In our model, longwave irradiance on the slopes,  $L$ , was calculated as in the following Equation (14):

$$L = L_0 + V_{\text{eff}} \varepsilon_s \sigma T_s^4, \quad (14)$$

where  $L_0$  is the observed incoming longwave radiation,  $V_{\text{eff}}$  is the effective terrain view factor (i.e. the difference between sky view factor at the observation site and that over the slope),  $\varepsilon_s$  is the emissivity of the surface (taken as 0.98),  $\sigma$  is the Stefan–Boltzmann constant ( $5.67 \times 10^{-8} \text{ W}/\text{m}^2/\text{K}^4$ ), and  $T$  is the surface temperature (K). We used the daily average air temperature as an approximation of the surface temperature. The parameter  $V_{\text{eff}}$  accounts for the fact that a component of the observed longwave radiation is contributed from adjacent terrain. This parameter effectively represents the relative increase (or decrease) in exposure to surrounding terrain, and thus provides a useful means for extrapolating longwave radiation measurements to nearby locations with different sky view factors. To obtain representative values of sky view factor within the cirque, several digital hemispheric photographs were taken over the two slopes and the floor of the cirque as well as at Fisera Ridge. Sky view factor was then calculated from these images, following Corripio (2003), as  $r^2/R^2$ , where  $r$  is the average radius of the visible horizon and  $R$  is the radius of the image.

The computed melt rates and accumulated melt over time were then used to simulate the SCD curves for the Mt. Allan cirque and for the north- and south-facing slopes within the cirque. These curves were generated by applying the accumulated melt over time to approximations of the observed SWE based on the lognormal distribution according to the theoretical framework described above. Observations from all surveys were used to characterize the overall distribution of SWE within the cirque. Observations from the northern part of survey #5 (Figure 1) were used to characterize the south-facing slope, whereas observations from surveys #2 and #3 and the southern part of survey #5 were used to characterize the north-facing slope (access to other parts of the slope was limited due to terrain hazards at that time). These surveys and the subsets of survey #5 seemed to represent the major features of the snowcover that were visibly apparent on both slopes; therefore, the sample observations are considered to be representative of the snowcover on both slopes at that time.

Because the month of April was characterized by further snow accumulation with cold temperatures and little or no snowmelt, the fitted SWE distributions were modified to account for an increase in  $\overline{\text{SWE}}$ . This was done by assuming that the values of CV from each of the surveys were conserved throughout the accumulation events, which is supported from observations in the sub-arctic (Pomeroy *et al.*, 2004) and from recent snow surveys on Fisera Ridge and within Mt. Allan cirque during the late winter and spring of 2008. Based on

this assumption, values of pre-melt standard deviation were recalculated using values of  $\overline{\text{SWE}}$  that had been adjusted to account for the additional accumulation that took place during the month of April. By Equation (2), this is equivalent to increasing the slope of the line in a plot of SWE versus  $K$ .

The effect of accumulation events in the melt period after the end of April was accounted for by using a rescaled depletion curve following Moore *et al.* (1999). After a snow accumulation event, the areal snowcover fraction was defined so as to revert to the initial maximum until a certain fraction of the new snow had melted (taken to be 0.5 in our model). A linear reversion to the original point on the SCD curve (e.g. when plotted as a function of  $K_{\min}$ ) occurred for the melt of the remainder of the new snow. This approach conceptually represents the fact that snowfall events during the spring are often wet and so less subject to wind redistribution via blowing snow as the threshold wind speed for transport is higher for wet snow (Li and Pomeroy, 1997). Therefore, spring snowfalls tend to produce a rather uniform distribution of snow over the landscape. For this reason, the Moore approach is considered to be superior to other reported techniques for handling snow accumulation (e.g. Luce *et al.*, 1999; Liston, 2004).

## RESULTS

### Pre-melt SWE distributions

Table II gives the statistical parameters of observed SWE values from all surveys conducted within and adjacent to the Mt. Allan cirque. The maximum  $\overline{\text{SWE}}$  value occurs for the mean of all surveys because these included several surveys with deeper snow (i.e. surveys #1 and #4 and parts of survey #5) that were not used to characterize the north- and south-facing slopes. The data from all surveys are shown in Figure 2, which plots values of observed SWE against the corresponding values of the frequency factor  $K$  (calculated by Equation (4)). A straight line representing the theoretical lognormal distribution is shown together with the observations of SWE within the cirque, and it is clear that the observed data deviate from this distribution considerably. It does appear, however, that SWE values plotted against  $K$  approximate a straight line for specific ranges of SWE, such as the more shallow depths of SWE up to  $\sim 700$

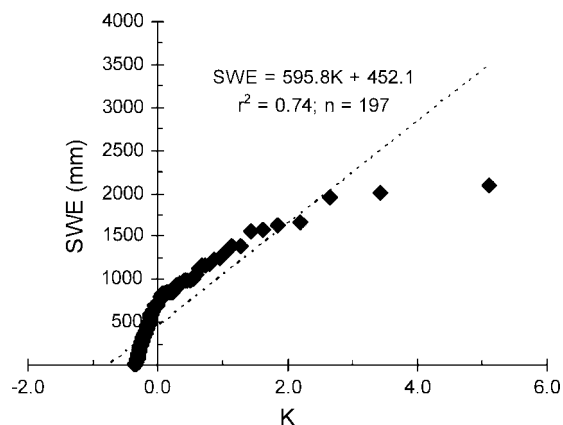


Figure 2. Pre-melt snow water equivalent (SWE) distribution for the Mt. Allan cirque based on surveys conducted on 29–30 March, 2007. Dashed line represents a theoretical lognormal distribution of SWE

mm, and some of the deeper snow from  $\sim 900$  to  $\sim 1500$  mm SWE.

SWE distributions over both the north- and the south-facing slopes are shown in Figure 3 and the statistical parameters of the observed SWE are given in Table II. The data show that stratification of observed SWE according to major terrain features produces a much better fit to the theoretical lognormal distribution. SWE values over the north-facing slope fit a straight line very well, particularly for shallow depths of SWE (Figure 3(a)). Over the south-facing slope, however, observed values of SWE still show deviations around the theoretical lognormal distribution, despite the fact that the linear fit to the data has been considerably improved from the combined SWE values for all surveys.

To attempt to obtain a better linear fit to the observed values of SWE over the south-facing slope, the data were divided into two categories: 'shallow' snow (i.e. SWE  $< 80$  mm) and 'deep' snow (i.e. SWE  $> 80$  mm). The measurements of SWE in these two categories more-or-less correspond to locations within the south-facing slope that are exposed and windswept, and areas that are sheltered and form drifts (i.e. surface depressions and small gullies). Observed SWE values are plotted against  $K$  for both the shallow and deep snow on the south-facing slope and shown in Figure 3(c) and (d). By distinguishing observed SWE in this manner, a strong linear fit is obtained for both the shallow and the deep snow over this slope, and the values of CV are significantly reduced (Table II).

### Observed areal SCD

Figure 4 shows several of the digital terrestrial photographs of the Mt. Allan cirque acquired during the snowmelt period, together with the georeferenced versions of these images. Previous studies have used oblique aerial photography for analysis of snowcover patterns in alpine terrain (e.g. Blöschl and Kirnbauer, 1992), but terrestrial-based photography allows for more frequent and consistent acquisition of imagery, and the procedure of Corripio (2004) is easily implemented with

Table II. Statistical parameters of observed SWE within the Mt. Allan cirque

Survey location	$\overline{\text{SWE}}$ (mm)	$s$ (mm)	CV
North-facing slope	329.3	318.3	0.97
South-facing slope	142.8	188.2	1.32
South-facing (shallow SWE)	24.6	13.4	0.54
South-facing (deep SWE)	339.8	178.7	0.53
All surveys	427.2	438.7	1.03

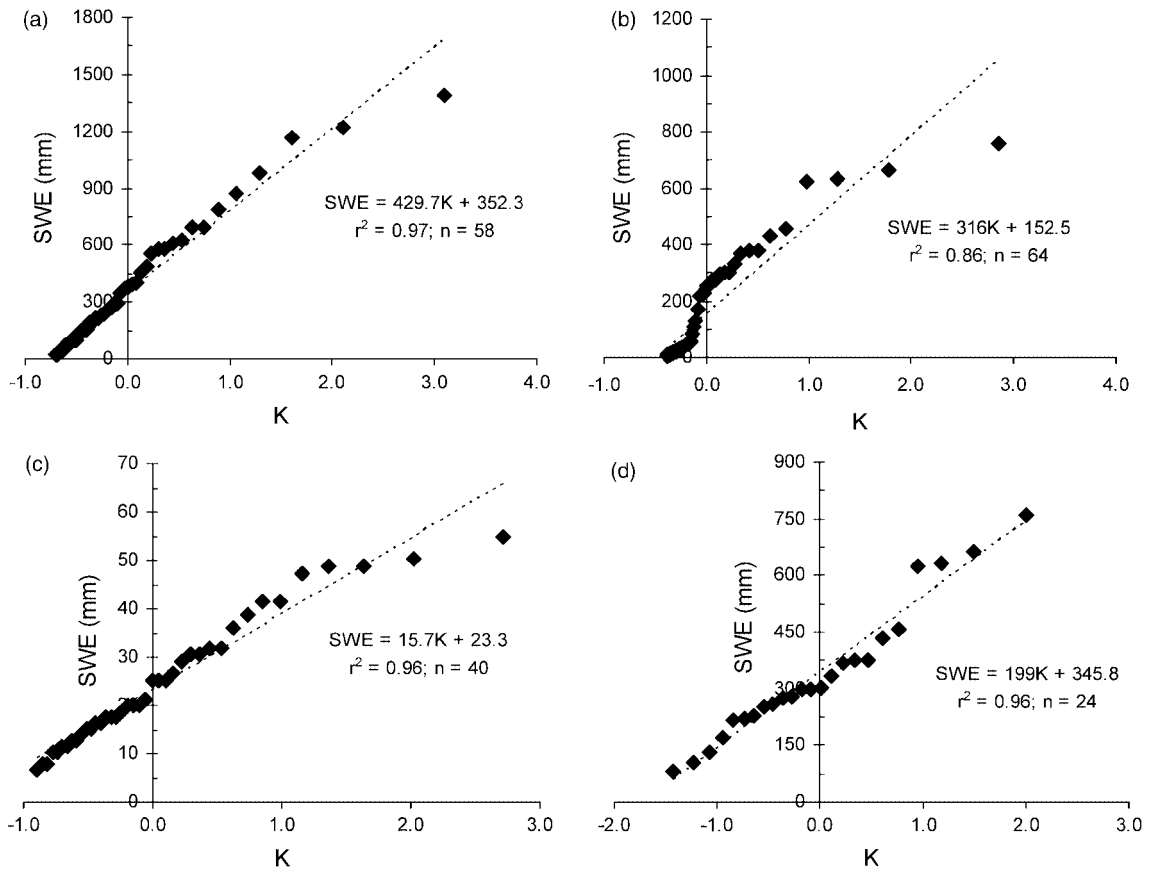


Figure 3. Pre-melt snow water equivalent (SWE) distributions for (a) north-facing and (b) south-facing slopes within the cirque as well as pre-melt SWE distributions for (c) 'shallow' and (d) 'deep' SWE over the south-facing slope, shown together with fitted theoretical lognormal distributions

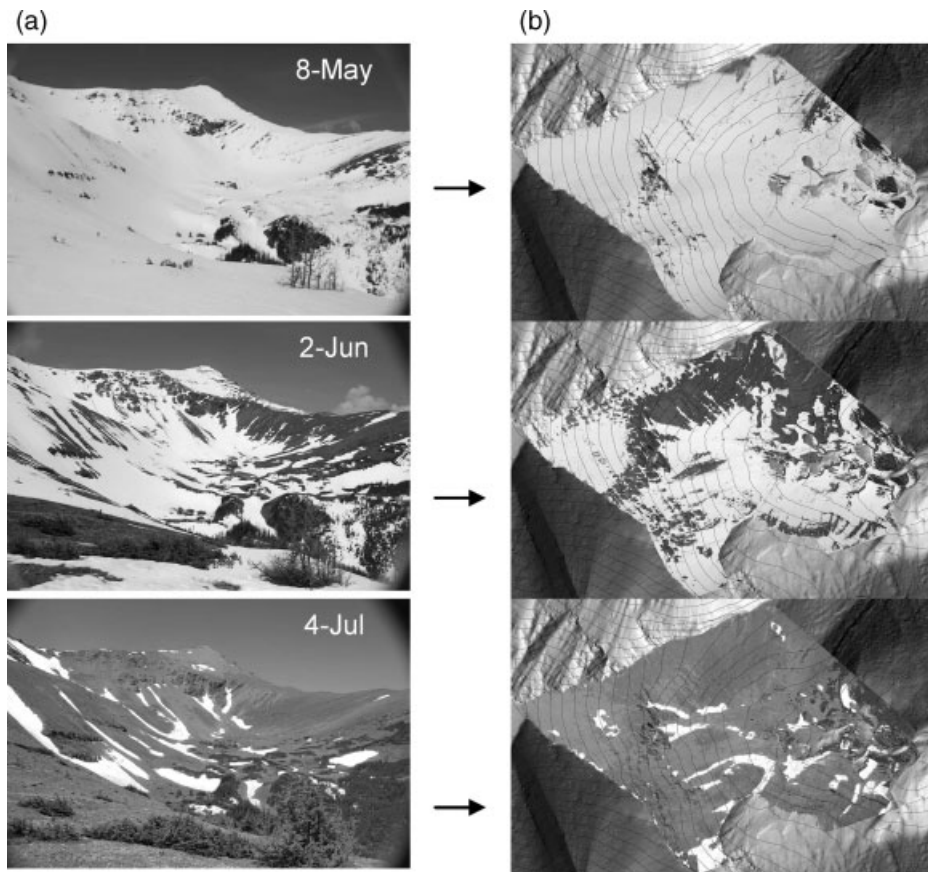


Figure 4. Examples of (a) original and (b) georeferenced terrestrial photographs of the Mt. Allan cirque at different times throughout the snowmelt period in 2007

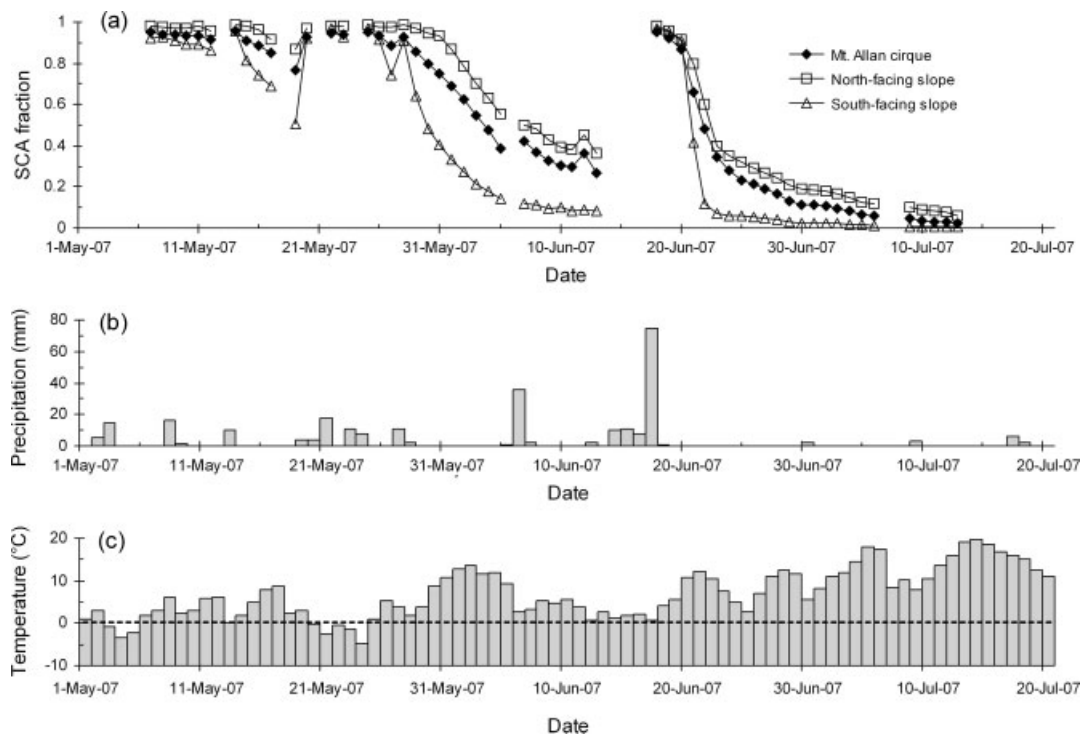


Figure 5. (a) Observed snowcover depletion curves for the entire Mt. Allan cirque and for the north- and south-facing slopes within the cirque, (b) total daily precipitation and (c) daily average air temperature at Fisera Ridge during the snowmelt period

accurate results. This imagery is very insightful as it shows how the snowcover disintegrated into a complex mosaic of snow patches and bare ground over time. The south-facing slope became predominantly snow-free much sooner than other parts of the cirque, including the north-facing slope. By early July, the only locations retaining snowcover were the depressions, gullies and lee slopes that formed drifts or accumulated deep snow during the winter.

The areal SCD curves that were obtained from the georeferenced terrestrial photography are shown in Figure 5(a) and indicate considerable differences in the timing and rate of SCD between the different slopes within the cirque. The primary period of snowmelt and SCD did not occur until mid to late May over much of the cirque, but this period began slightly earlier on the south-facing slope and progressed much faster here. Periods of cool weather and intermittent snowfall events (Figure 5(b)) kept melt rates low and frequently renewed the snowcover over the entire cirque until a period of warm and sunny weather in late May and early June, when high melt rates led to rapid rates of SCD. Another major snowfall event occurred in mid-June, which blanketed the entire cirque with nearly 80 mm water equivalent of fresh snow. As this snow melted during the following days, SCD rates were at first low and became increasingly rapid with warming temperatures and greater fractions of exposed ground. The SCD curves following this event then gradually approached the original curves as the more recent snow disappeared and the remaining areas of deeper snow became progressively depleted until mid or late July.

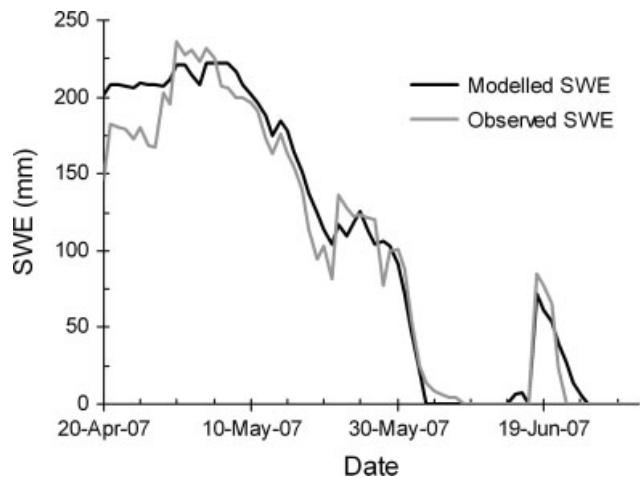


Figure 6. Comparison of modelled snow water equivalent (SWE) using cold regions hydrological model together with Snobal and observed SWE values at the Fisera Ridge meteorological station

#### Simulated snowmelt and SCD

Figure 6 shows both the modelled and observed SWE at the Fisera Ridge meteorological station. SWE was modelled for this test case using an initial value of 170 mm SWE depth beginning on 1 April. Observed SWE values were derived from the measurements of snow depth obtained from the SR50, together with measured snow density at several times throughout the melt period and estimated density (i.e. interpolated between measurements and adjusted for new snow by assuming a fresh snow density of  $150 \text{ kg/m}^3$ ) for the intervening periods. The model clearly performs well for the simulation of snowmelt, as it accurately represents the timing of

both melt onset and snow disappearance, and conforms well to the observed melt rates at all times during the snowmelt period. The model also performs reasonably well in simulating snow accumulation, but does have the tendency to misrepresent short-term variability, which is likely due to snow redistribution and drifting. Table III gives the RMS error between modelled and observed SWE (excluding times when SWE = 0). The evaluation of the model at a point confirms that it is suitable for simulations of snowmelt at Fisera Ridge, and represents an important step towards applying it over other remote areas within the cirque.

Simulated daily melt rates for the two opposing slopes are shown in Figure 7(a), whereas Figure 7(b) and (c) shows the modelled shortwave and longwave radiation inputs that were partially driving simulated melt rates over the two slopes. Melt rates simulated by the model were relatively low or zero throughout April and much of early May, and became greater in magnitude in late May/early June, and again in late June and throughout July. During most of the spring, the south-facing slope was characterized by higher melt rates as a result of

greater incident solar radiation. Towards the summer solstice, melt rates became similar in magnitude between the north- and south-facing slopes because of high solar angles, longer daylight hours and a longer solar path with more northerly solar azimuths in the morning and late afternoon. Due to the greater exposure to surrounding terrain, modelled incident longwave radiation to the north-facing slope was greater throughout the spring. Thus, at times when conditions were cloudy and long-wave radiation contributed a relatively greater proportion of the total melt energy, simulated melt rates became comparable between the slopes, or even greater on the north-facing slope. Over the duration of the simulation period (i.e. 1 April to 20 July, 2007), total incoming shortwave radiation to the south-facing slope was ~751 MJ/m<sup>2</sup>, or 36% greater than that to the north-facing slope, whereas total longwave radiation was ~134 MJ/m<sup>2</sup>, or 4% greater to the north-facing than to the south-facing slope. Total potential accumulated melt over the south-facing slope was 316 mm, or 19% greater than that over the north-facing slope as a result of the net incoming radiation difference.

Simulated melt rates based on the observed meteorological conditions at Fisera Ridge were used together with the theoretical lognormal distribution of SWE in Figure 2 to generate the SCD curve shown in Figure 8(a). This curve clearly fails to capture the timing and rate of areal SCD over the cirque. The modelled SCD curve does not begin to decline until nearly 2 weeks after observed SCD began in late May, and once this does begin to occur, the rate of depletion is far too rapid during the first several days. The initial phase of minor SCD during the early

Table III. RMS errors between measurements and simulations of SWE and fractional SCA

Simulation	RMS error
Fisera Ridge SWE	18.4 mm
Mt. Allan cirque SCA	0.20
North-facing slope SCA	0.08
South-facing slope SCA	0.15
South-facing slope SCA (after 20 May)	0.10

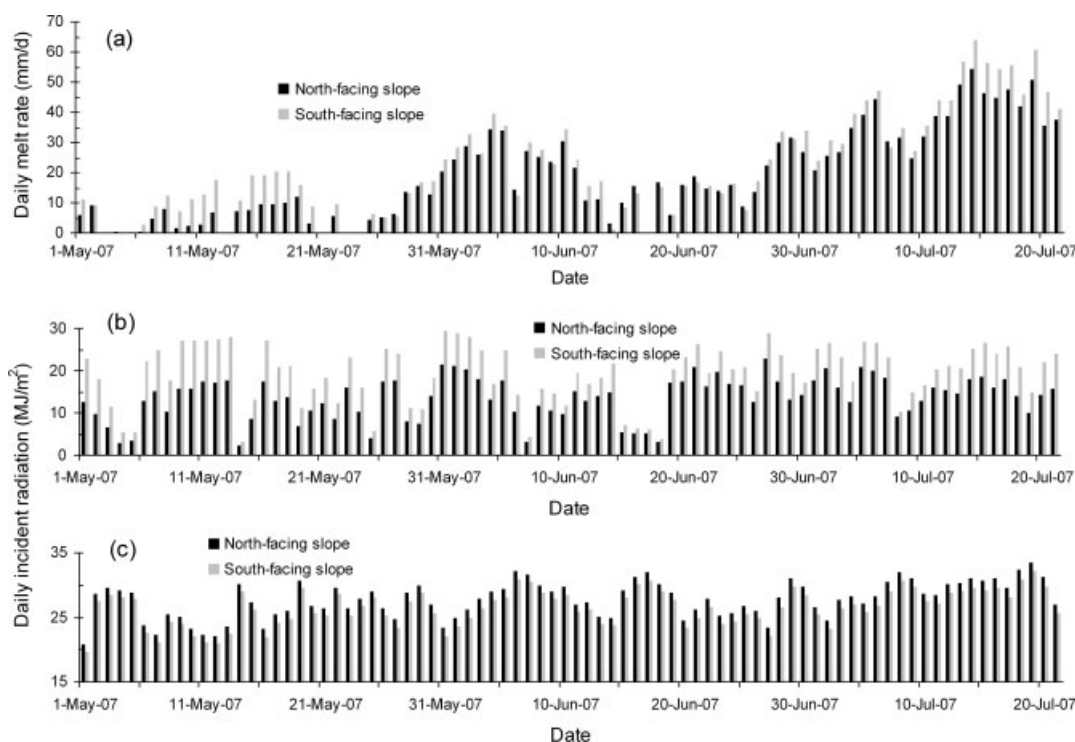


Figure 7. (a) Simulated daily melt rates for the north- and south-facing slopes within the Mt. Allan cirque; (b) simulated values of total daily incident shortwave radiation for both slopes; and (c) simulated values of total daily incident longwave radiation for both slopes

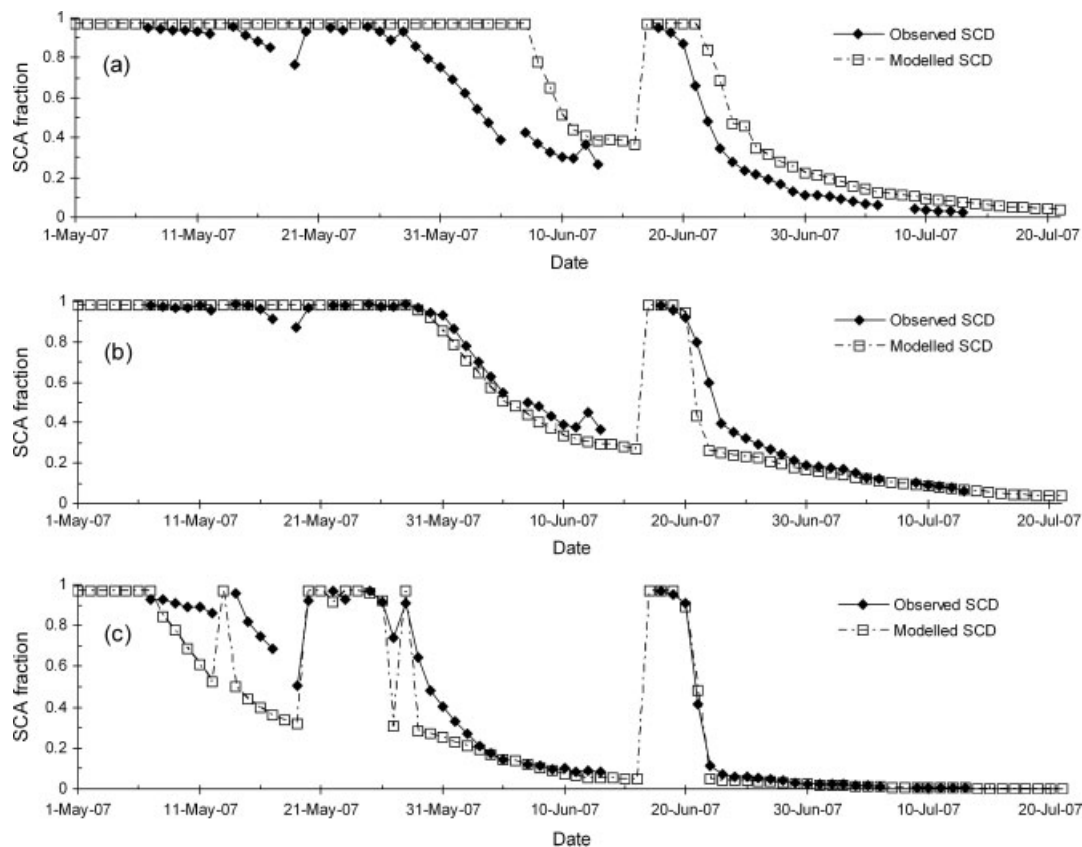


Figure 8. Observed and modelled snowcover depletion curves for (a) the spatially lumped representation of the Mt. Allan cirque, (b) the north-facing slope and (c) the south-facing slope

melt period is missed by the model, and the SCD curve takes too long to decline during the late melt period.

The modelled SCD curves for both the north- and the south-facing slopes were similarly generated using the corresponding distributions of SWE and the simulated melt rates for both slopes. The SCD curve for the south-facing slope was derived by making separate calculations of fractional SCA over time for each of the two fitted distributions (i.e. Figure 3(c) and (d)), and subsequently weighting the calculations of SCA by the relative proportion of the sample observations in each category (i.e. 62.5% and 37.5% for 'shallow' and 'deep' SWE, respectively). The results in Figure 8(b) and (c) and Table III indicate that by treating initial SWE distributions and melt rates separately over the two slopes, the model performs far better at predicting fractional SCA, and the timing and rate of simulated SCD are substantially improved. The approach used for rescaled SCD following snow accumulation events has also produced a good correspondence with the observed SCD at these times. Despite the improvements, however, the results of the model still suffer some errors, particularly during the early snowmelt period over the south-facing slope.

## DISCUSSION

### *Spatial variability of snowmelt and SWE*

The results show that the SWE values from surveys from several distinct slope units, when grouped together,

are not well represented by the lognormal distribution. This is in concurrence with Pomeroiy *et al.* (2004) who found the lognormal distribution failed when snow surveys were aggregated over several terrain classes in a Yukon mountain environment, but worked well when snow surveys were stratified by terrain following Stephun and Dyck (1974). When a lognormal approximation is fitted to the aggregated snow survey data and used to predict the decline in areal snowcover over the spring, the results are subject to considerable error and do not conform well to observations. This is due either to deviation of the SWE values from the lognormal distribution, spatial variability of snowmelt rates within the cirque or some combination of both. Figure 2 shows that the lognormal approximation of the observed values of SWE overpredicts these values at low values of  $K$  (i.e.  $< -0.2$ ), which correspond to observed values of SWE  $< 350$  mm and  $P(\text{SWE}) > 0.43$ . A significant portion of the total SWE distribution is therefore misrepresented, which would lead to an overestimation of areal snowcover as this snow melted and disappeared. The observed  $K_{\min}$  for the distribution is  $-0.36$ , where the fitted curve predicts a SWE value of 215 mm (Figure 2). This indicates that 215 mm of accumulated melt is required to produce any decline in SCA. Based on our assumption that the CV is conserved, however, the actual required melt depth is even greater as the slope of the line was increased to account for the increase in  $\overline{\text{SWE}}$ . According to the model, a net accumulated melt depth of 262 mm

had occurred before the predicted areal snowcover began to decline. This is an obvious error that is directly attributable to the poor fit of observed SWE values to the lognormal distribution, and explains why modelled SCD does not begin until late in the snowmelt period.

Due to similar misrepresentation of observed SWE by the lognormal distribution over all ranges of  $K$ , it is difficult to infer the magnitude of errors that may be due to any spatial variability in snowmelt over the cirque. It is noted that late in the melt period, the rate of modelled SCD began to more closely approximate the observed rate of depletion, despite a delay of several days (Figure 8(a)). This is possibly due to a closer approximation of SWE over the range of  $K$  from  $-0.1$  to  $2.0$ , together with increasingly uniform melt rates over the cirque with time. It is more likely, however, that this is a result of the cancellation of multiple errors in the modelling procedure producing realistic appearing results, but for the wrong reasons.

A significant improvement in the results was achieved by separately treating initial SWE distributions and melt rates for the two slopes within the cirque. Based on the close fit of observed SWE values to the theoretical lognormal distribution (when stratified by terrain features) and the specific modelling approach used in this study, which assumed uniform melt energy receipt by slope unit, the results suggest that the variability in both pre-melt SWE and melt energetics over differing slopes has a major effect on areal SCD in this environment. The differences between the initial distributions of SWE over the two slopes are attributed to factors such as the direction of prevailing winds on blowing snow transport and redistribution over local topography and the effect of differences in energy receipt over the winter on the energetics of ablation on the north- and south-facing slopes. An interesting result is that 'shallow' and 'deep' snow over the south-facing slope can be treated separately to reduce the CV of SWE and further improve the lognormal fit to the observations. This implies that small-scale (i.e. 1–100 m) snow wind redistribution processes may have a large impact on the overall distribution of SWE within individual slope units. Similar results were not found for the north-facing slope, possibly due to differences in wind-loading. The fact that the modelled SCD curve closely approximated the observed curve attests that the single approximated frequency distribution can sufficiently represent the snowcover on this slope when snowcover is stratified by terrain features.

Melt rate differences at this scale are primarily related to differences in radiation receipt as influenced by topography. These differences are primarily a result of differential receipt of shortwave radiation between slopes, which in the Rocky Mountain Front Ranges and similar environments is relatively pronounced in contrast with more humid and cloudy environments. The effect of differences in the exposure to surrounding terrain on longwave radiation also has an important effect on melt energetics. The approach used here approximated the temperature of the surrounding terrain using mean daily air temperature, but

differences in the effective surface temperature of the terrain that slope units are exposed to could lead to further variation in longwave irradiance over the cirque. Exposed soil, rocks and vegetation can be significantly warmer than melting snow ( $\leq 0^\circ\text{C}$ ), especially during clear days. For example, in the spring of 2008 when the snowcover was near maximum spatial extent, we measured temperatures of exposed rocks in the cirque of more than  $22^\circ\text{C}$  using a thermal infrared camera. Thus, as different parts of the cirque become free of snow at different rates and times, the effect could be to increase, or alternatively dampen, the spatial variation in longwave irradiance over different parts of the cirque.

Despite the improvements, the modelled SCD curves still exhibit some obvious errors. On the north-facing slope, the minor reductions in SCA in mid-May were not well simulated, whereas on the south-facing slope, the magnitude of SCA was greatly underestimated during the early melt period. These features are likely due to misrepresentations of the actual distributions of SWE on the slopes at these specific times. For example, our approach was to adjust the pre-melt SWE distributions by assuming that CV values are conserved while  $\overline{\text{SWE}}$  increases in the early spring. This assumption may not entirely hold, and may be responsible for some of the errors in the early stages of areal SCD. The fitting method used to estimate the parameters for this distribution is biased towards estimating the mean of the distribution rather than the tails. This would have the largest impact over the south-facing slope, where a large percentage of the terrain is exposed and windswept, and represented by a distribution with a very low value of  $\overline{\text{SWE}}$ . Furthermore, the shallow snow on much of this slope is highly transient and likely more difficult to represent based on the approach used here. This may partly explain the large deviations between modelled and observed SCD curves on this slope in the early melt period, and it is possible that an improved physical basis for representing snow redistribution following accumulation events would result in an improvement of the simulated curve.

Another possible cause of the poor model performance in the early simulation period may include spatial variability in snowmelt at scales smaller than the individual slopes. This could result from small-scale advection of sensible heat from adjacent areas of bare ground, exposed rocks and vegetation as well as local variations in incident solar radiation due to small variations in microtopography. Both sources of variation would be relatively more important over the south-facing slope due to the greater amount of incident solar radiation. Local advection of energy could result in significant enhancement of snowmelt in certain locations as SCA declines (Marsh *et al.*, 1997; Shook and Gray, 1997; Granger *et al.*, 2002). It is unclear over what spatial scales this process operates in this environment, thus implying the need for further investigation on the relative importance of advection on snowmelt. The effects of variable SWE at small scales may also be important in terms of variable melt rates due

to variable internal energy storage. This point is discussed further below.

### Modelling implications

The results of this study indicate that at the scale of individual slope units in this particular environment (i.e.  $\sim 100$ – $500$  m), there are spatial variations in both the distributions of pre-melt SWE and the melt rates applied to these distributions. This variability strongly influences the timing and rate of areal SCD, and the SCD curve is not adequately represented by considering only the overall (basin scale) distribution of SWE and spatially uniform melt rates, in accordance with the findings of Dornes *et al.* (2008) for sub-arctic complex terrain. Related work on the effects of variability in pre-melt SWE and melt rates in mountainous terrain has shown that both sources of variation are important for accurate representation of areal SCD and meltwater runoff generation (e.g. Tarboton *et al.*, 2000 and references therein). These previous studies as well as the present study have demonstrated that simply applying effective, or basin average parameters results in large errors; this is due to the nonlinear nature of snowmelt processes (Blöschl, 1999). However, in these other studies, the optimal results were only achieved by the use of a fully distributed model. In this study, we have shown that such an approach was not necessary to achieve a good correspondence between observations and model results. Rather, we have used objective means to stratify the terrain, and in so doing, were able to account explicitly for the major sources of variability in the radiative components of snowmelt energetics over the landscape. Dornes *et al.* (2008) also showed that this works in sub-arctic mountainous landscapes. At smaller spatial scales (i.e. below that of the individual slope units), we have accounted for the variability in SWE using a stochastic approach based on the theoretical lognormal distribution, and therefore simulated SCA and SCD with accuracy. This is ideal because the parameters for this distribution can likely be determined from a limited number of snow surveys based on representative landforms (e.g. Pomeroy *et al.*, 1998). Such simulations have not been done successfully before in complex terrain without resorting to highly parameterized, fully distributed models, and shows that simpler modelling strategies that employ both top-down understanding of system behaviour and bottom-up representation of physical processes can have considerable success (Dornes *et al.*, 2008; Savenije, 2009).

These results suggest that the appropriate scale for disaggregation of the terrain depends on the associated scale dependence of the variability of both SWE and melt rates. In similar environments, large variations in snowmelt energetics due to variations in radiation receipt, as well as air temperature variation with elevation, are likely to occur at the scale of the individual slope units (e.g.  $\sim 100$ – $500$  m length scale in this case). Distinct distributions of SWE are likely to become obscured and distorted beyond such scales as homogeneous slope units are combined, but this may occur at much smaller scales

in some instances. Therefore, this scale seems to be an upper limit for modelling applications, beyond which explicit spatial representation is necessary, and within which small-scale variability may be represented stochastically. However, the appropriate landscape stratification is not only scale-dependent (e.g. Cline *et al.*, 1998) but also location dependent, so as to conform to the underlying variations in terrain (i.e. distinct units of slope/aspect, exposure and elevation) that are responsible for the variation in snow processes.

In this environment, snowmelt is frequently interrupted by snowfall events that refresh the snowcover and delay melt to some extent. These events must be properly accounted for to produce reasonable simulations of snowmelt and SCD. Although the method of Moore *et al.* (1999) is not physically based, it performs well in simulating the areal depletion of snow over the periods immediately following snowfall events. Other published approaches would have either resulted in too rapid an areal depletion of snowcover (e.g. by failure to account for reduced wind redistribution of snow and prediction of an immediate decline in SCA; Luce *et al.*, 1999), or would have failed to restore the snowcover to its maximum value following snowfall events (e.g. by assuming SCA to follow the same depletion curve regardless of such accumulation events; Liston, 2004). The albedo refresh and decay parameterization given by Essery and Etchevers (2004) has also been found to work well following snowfall events.

The finding that an improved linear fit to the SWE observations is achieved when snow on the south-facing slope is stratified by depth of SWE into exposed and sheltered terrain has influenced the modelling procedure employed and has had a large influence on the results. It is likely that this may be an important feature of the snowcover on other, predominantly windswept slopes in this environment and other windy alpine regions. Therefore, an objective means of classifying the exposed versus the sheltered terrain may need to be employed in circumstances where detailed snow measurements (e.g. surveys or remotely sensed imagery) are lacking. This could include indices such as terrain slope or curvature, which are useful surrogates for zones of drift formation (Tabler, 1975; Blöschl *et al.*, 1991; Liston and Sturm, 1998), or more detailed indices taking into account upslope length and terrain curvature in the direction of prevailing winds (e.g. Winstral and Marks, 2002).

An issue remains in that it may be problematic to simulate uniform melt rates over a nonuniform snowcover that is characterized by large differences in depth and density over short distances. The internal energetics (i.e.  $dU/dt$ ) of the snowpack are dependent on snow depth, density and temperature, which may all exhibit differing degrees of spatial variance and covariance. Simulating an areal snowcover by applying point-scale simulations that rely only on areal mean values may therefore introduce deviations from reality due to the effects of this variation (Horne and Kavvas, 1997). This issue could perhaps be resolved by considering separate classes of SWE depth

for melt rate computation within individual slope units. The approach is similar to disaggregating the slope into exposed and sheltered areas for improving the linear fit to the observed SWE values, and weighting relative proportions of the slope by the areal extent of these zones. An ideal solution is to compute melt rates separately over the same subsets of the total SWE distribution used to define exposed and sheltered terrain. Alternatively, a stochastic approach may be necessary to simulate melt rate variability and its effects on SCD as a result of covariance between the joint SWE and melt rate distributions (Essery and Pomeroy, 2004; Pomeroy *et al.*, 2001).

Improvements in simulations might also result from a more accurate representation of the temporal variation in melt energetics, so that towards the later stages of the snowmelt period, sufficient melt rates are applied to simulate the depletion of the remaining snow in sheltered areas such as snowdrifts and snow-filled gulleys. This is linked to improved spatial representation of melt as it is controlled by the spatial distribution of pre-melt SWE. During the pre-melt period, energy inputs to the deeper and denser snow in these areas are used to warm the snowpack up to 0°C, while energy inputs to adjacent areas of shallow isothermal snowcover are more likely to be expended in snowmelt. In the later stages of the melt period, the remaining snow in sheltered areas is subjected to greater energy inputs than those applied earlier in melt due to advection of sensible heat from local bare ground, warmer air masses, longer daylight periods and significantly reduced snow albedo as a result of wind-blown debris, snow algae, etc., that have accumulated on the snow surface. The fact that we allowed the surface albedo in our model to decline towards a value of 0.3 in the late melt period has likely accounted for differences in energetics in later melt and the increase in melt rates by advection to late-lying snow patches. Further work is required to elucidate the effects of such spatial and temporal variations in snowmelt on large scale SCD curves.

## CONCLUSIONS

This study examined the spatial variability in areal depletion of the snowcover over a small alpine cirque in the Front Ranges of the Canadian Rocky Mountains during the spring of 2007. The approach consisted of direct observation using oblique terrestrial photography, together with SCD simulation based on measured pre-melt distributions of SWE and point-scale snowmelt modelling using observed meteorological conditions at the cirque. The results of the model were found to be in reasonable agreement with both the observations of SWE at the meteorological station and the timing and rate of SCD over two opposing slopes within the cirque. The key findings and implications of this research are the following:

1. Distributions of SWE before the onset of melt fit the theoretical lognormal distribution function well

when stratified by major terrain features such as slope orientation and topographic exposure.

2. Spatial variation in surface energetics resulting from differences in radiation receipt due to differential slope orientation and sky/terrain view has a significant effect on snowmelt rates and areal SCD at the scale of individual slope units.
3. Prediction of the timing and rate of areal SCD is significantly improved when the simulation procedure accounts for the difference in both pre-melt SWE distributions and the radiative components of snowmelt energetics that occur between slopes.
4. The scale and spatial extent of individual slope units (i.e. ~100–500 m length scale for this particular basin) in complex alpine environments likely represent an upper limit for model applications dealing with areal SCD, with major variations in radiative components of snowmelt energetics represented explicitly, and variability in SWE within these units represented stochastically.
5. Terrestrial photography provides a reliable and useful means of deriving high-resolution and high-frequency imagery for environmental monitoring in alpine areas where conventional remote sensing techniques are unfeasible.

Further work needs to address several remaining issues. One issue involves the effects of small-scale spatial variability in pre-melt SWE and melt energetics on SCD within individual slope units. The implications of applying uniform melt rates should be more rigorously assessed through a combined modelling and observation approach. Furthermore, the representativeness of limited snow surveys for estimates of  $\overline{\text{SWE}}$  and CV over more broad parts of the landscape should be demonstrated. Repeat measurements using airborne LiDAR (e.g. with and without snowcover) provide an ideal tool that has not yet been fully used in this context. This will also provide insight into the extent to which the landscape must be disaggregated to achieve distinct SWE distributions. Future model applications can then use these findings to couple over-winter snow accumulation and redistribution processes with snowmelt processes, and thereby improve simulations of the overall basin scale SCA and SCD.

## ACKNOWLEDGEMENTS

Funding for this work was provided by the Canadian Foundation for Climate and Atmospheric Sciences (CFCAS) through their support of the IP3 Research Network, the Natural Sciences and Engineering Research Council of Canada (NSERC), the University of Calgary Biogeoscience Institute and the Canada Research Chairs program. Nakiska Ski Resort kindly provided logistical support. The authors gratefully acknowledge the field assistance of Richard Essery (Univ. Edinburgh), Greg Langston (Univ. Calgary), Chad Ellis, Matt MacDonald and Jim MacDonald (Univ. Sask). We also thank Michael

Solohub (Univ. Sask) for technical support with the camera and meteorological stations and for help in the field, Javier Corripio (Univ. Innsbruck) for helpful instruction on the setup of the camera, Kevin Shook (Univ. Sask) for insightful discussion on the lognormal frequency distribution and SCD calculation and Tom Brown (Univ. Sask) for CRHM development and support. Two anonymous reviewers provided comments that greatly improved the manuscript.

## REFERENCES

- Allen TR, Walsh SJ. 1993. Characterizing multitemporal alpine snowmelt patterns for ecological inferences. *Photogrammetric Engineering and Remote Sensing* **59**: 1521–1529.
- Anderton SP, White SM, Alvera B. 2004. Evaluation of spatial variability in snow water equivalent for a high mountain catchment. *Hydrological Processes* **18**: 435–453.
- Blöschl G. 1999. Scaling issues in snow hydrology. *Hydrological Processes* **13**: 2149–2175.
- Blöschl G, Kirnbauer R. 1992. An analysis of snow cover patterns in a small alpine catchment. *Hydrological Processes* **6**: 99–109.
- Blöschl G, Kirnbauer R, Gutknecht D. 1991. A spatially distributed snowmelt model for application in alpine terrain. In *Snow, Hydrology and Forests in High Alpine Areas, Proceedings of the Vienna Symposium*, August 1991, Bergmann H, Lang H, Frey W, Issler D, Salm B (eds). IAHS publication No. 205, IAHS: Wallingford; 51–60.
- Chow VT. 1954. The log-probability law and its engineering applications. *Proceedings of the American Society of Civil Engineers* **80**: 1–25.
- Cline D, Elder K, Bales R. 1998. Scale effects in a distributed snow water equivalence and snowmelt model for mountain basins. *Hydrological Processes* **12**: 1527–1536.
- Corripio JG. 2003. Vectorial algebra algorithms for calculating terrain parameters from DEMs and solar radiation modelling in mountainous terrain. *International Journal of Geographic Information Science* **17**: 1–23.
- Corripio JG. 2004. Snow surface albedo estimation using terrestrial photography. *International Journal of Remote Sensing* **25**: 5705–5729.
- Davis RE, McKenzie JC, Jordan R. 1995. Distributed snow process modelling: An image processing approach. *Hydrological Processes* **9**: 865–875.
- Davison B, Pohl S, Dornes P, Marsh P, Pietroniro A, MacKay M. 2006. Characterizing snowmelt variability in a land-surface-hydrologic model. *Atmosphere-Ocean* **44**: 271–287.
- Donald JR, Soulis ED, Kouwen N, Pietroniro A. 1995. A land cover-based snow cover representation for distributed hydrologic models. *Water Resources Research* **31**: 995–1009.
- Dornes PF, Pomeroy JW, Pietroniro A, Carey SK, Quinton WL. 2008. Influence of landscape aggregation in modelling snow-cover ablation and snowmelt runoff in a sub-arctic mountainous environment. *Hydrological Sciences Journal* **53**: 725–740.
- Elder K, Dozier J, Michaelsen J. 1991. Snow accumulation and distribution in an alpine watershed. *Water Resources Research* **27**: 1541–1552.
- Elder K, Rosenthal W, Davis R. 1998. Estimating the spatial distribution of snow water equivalence in a montane watershed. *Hydrological Processes* **12**: 1793–1808.
- Essery R, Etchevers P. 2004. Parameter sensitivity in simulations of snowmelt. *Journal of Geophysical Research* **109**: D20111. DOI: 10.1029/2004JD005036.
- Essery RH, Pomeroy JW. 2004. Implications of spatial distributions of snow mass and melt rate for snow-cover depletion: theoretical considerations. *Annals of Glaciology* **38**: 261–265.
- Faria DA, Pomeroy JW, Essery RH. 2000. Effect of covariance between ablation and snow water equivalent on depletion of snow-covered area in a forest. *Hydrological Processes* **14**: 2683–2695.
- Garnier BJ, Ohmura A. 1970. The evaluation of surface variations in solar radiation income. *Solar Energy* **13**: 21–34.
- Granger RJ, Pomeroy JW, Parviainen J. 2002. Boundary-layer integration approach to advection of sensible heat to a patchy snow cover. *Hydrological Processes* **16**: 3559–3569.
- Gumbel EJ. 1954. *Statistical Theory of Extremes and Some Practical Applications*. U.S. National Bureau of Standards Applied Mathematics Series 33, U.S. Govt. Printing Office: Washington, DC.
- Hartman MD, Baron JS, Lammers RB. 1999. Simulations of snow distribution and hydrology in a mountain basin. *Water Resources Research* **35**: 1587–1603.
- Horne FE, Kavvas ML. 1997. Physics of the spatially averaged snowmelt process. *Journal of Hydrology* **191**: 179–207.
- Li L, Pomeroy JW. 1997. Estimates of threshold wind speeds for snow transport using meteorological data. *Journal of Applied Meteorology* **36**: 205–213.
- List RJ. 1968. *Smithsonian Meteorological Tables*, 6th ed. The Smithsonian Institution: Washington, DC; 527 pp.
- Liston GE. 1999. Interrelations among snow distribution, snowmelt, and snow cover depletion: Implications for atmospheric, hydrologic, and ecologic modeling. *Journal of Applied Meteorology* **38**: 1474–1487.
- Liston GE. 2004. Representing subgrid snow cover heterogeneities in regional and global models. *Journal of Climate* **17**: 1381–1395.
- Liston GE, Sturm M. 1998. A snow-transport model for complex terrain. *Journal of Glaciology* **44**: 498–516.
- Luce C, Tarboton D. 2004. The application of depletion curves for parameterization of subgrid variability of snow. *Hydrological Processes* **18**: 1409–1422.
- Luce CH, Tarboton DG, Cooley KR. 1999. Sub-grid parameterization of snow distribution for an energy and mass balance snow cover model. *Hydrological Processes* **13**: 1921–1933.
- Marks D, Domingo J, Susong D, Link T, Garen D. 1999. A spatially distributed energy balance snowmelt model for application in mountain basins. *Hydrological Processes* **13**: 1935–1959.
- Marks D, Kimball J, Tingey D, Link T. 1998. The sensitivity of snowmelt processes to climate conditions and forest cover during rain-on-snow: A case study of the 1996 Pacific Northwest flood. *Hydrological Processes* **12**: 1569–1587.
- Marks D, Winstral A. 2001. The effect of variable patterns of snow deposition and drifting on snowmelt, runoff, and stream discharge in a semi-arid mountain basin. In *Proceedings of the Western Snow Conference, 69th*, 16–19 April 2001, Sun Valley, Idaho; 127–130.
- Marsh P, Pomeroy JW, Neumann N. 1997. Sensible heat flux and local advection over a heterogeneous landscape at an Arctic tundra site during snowmelt. *Annals of Glaciology* **25**: 132–136.
- Moore RJ, Bell VA, Austin RM, Harding RJ. 1999. Methods for snowmelt forecasting in upland Britain. *Hydrology and Earth System Sciences* **3**: 233–246.
- Pomeroy J. 1991. Transport and sublimation of snow in wind-scoured alpine terrain. In *Snow, Hydrology and Forests in High Alpine Areas, Proceedings of the Vienna Symposium, August 1991*, Bergmann H, Lang H, Frey W, Issler D, Salm B (eds). IAHS publication No. 205, IAHS: Wallingford; 131–140.
- Pomeroy JW, Essery RH, Toth B. 2004. Implications of spatial distributions of snow mass and melt rate for snow-cover depletion: Observations in a subarctic mountain catchment. *Annals of Glaciology* **38**: 195–201.
- Pomeroy JW, Gray DM, Brown T, Hedstrom NR, Quinton WL, Granger RJ, Carey SK. 2007. The cold regions hydrological process representation and model: A platform for basing model structure on physical evidence. *Hydrological Processes* **21**: 2650–2667.
- Pomeroy JW, Gray DM, Shook KR, Toth B, Essery RLH, Pietroniro A, Hedstrom N. 1998. An evaluation of snow accumulation and ablation processes for land surface modelling. *Hydrological Processes* **12**: 2339–2367.
- Pomeroy JW, Hanson S, Faria DA. 2001. Small-scale variation in snowmelt energy in a boreal forest: An additional factor controlling depletion of snow cover? In *Proceedings of the Eastern Snow Conference, 58th*, 14–17 May 2001, Ottawa, Ontario, 85–96.
- Pomeroy JW, Toth B, Granger RJ, Hedstrom NR, Essery RH. 2003. Variation in surface energetics during snowmelt in a subarctic mountain catchment. *Journal of Hydrometeorology* **4**: 702–718.
- Savenije HHG. 2009. The art of hydrology. *Hydrology and Earth System Sciences* **13**: 157–161.
- Seyfried MS, Wilcox BP. 1995. Scale and the nature of spatial variability: Field examples having implications for hydrologic modelling. *Water Resources Research* **31**: 173–184.
- Shook KR. 1995. *Simulation of the ablation of prairie snowcovers*. PhD thesis, University of Saskatchewan, 189 pp.
- Shook KR, Gray DM. 1997. Snowmelt resulting from advection. *Hydrological Processes* **11**: 1725–1736.
- Sicart JE, Pomeroy JW, Essery RLH, Bewley D. 2006. Incoming longwave radiation to melting snow: Observations, sensitivity and estimation in northern environments. *Hydrological Processes* **20**: 3697–3708.

- Steppuhn HW, Dyck GE. 1974. Estimating true basin snowcover. In *Advance Concepts in Technical Study of Snow and Ice Resources, Interdisciplinary Symposium*. U.S. National Academy of Science: Washington, DC; pp 314–328.
- Storr D. 1967. Precipitation variations in a small forested watershed. In *Proceedings of the Annual Western Snow Conference*, 35th, 18–20 April 1967, Boise, Idaho; 11–17.
- Tabler RD. 1975. Predicting profiles of snowdrifts in topographic catchments. In *Proceedings of the Annual Western Snow Conference*, 43rd, 23–25 April 1975, Coronado, California; 87–97.
- Tarboton D, Blöschl G, Cooley K, Kirnbauer R, Luce C. 2000. Spatial snow processes at Kütai and Reynolds Creek. In *Spatial Patterns in Catchment Hydrology: Observations and Modelling*, Grayson R, Blöschl G (eds). Cambridge University Press: Cambridge, UK; 158–186.
- Winstral A, Marks D. 2002. Simulating wind fields and snow redistribution using terrain-based parameters to model snow accumulation and melt over a semi-arid mountain catchment. *Hydrological Processes* **16**: 3585–3603.